Supplemental Information for Direct Measurement of the Singlet Lifetime and Photoexcitation Behavior of the Boron Vacancy Center in Hexagonal Boron Nitride

Richard A. Escalante*†[1,2], Andrew J. Beling*‡[1,3], Daniel G. Ang[1], Niko R. Reed[1,3,4], Justin J. Welter[1,2], John W. Blanchard[1], Cecilia Campos[5], Edwin Coronel[5], Klaus Krambrock[6], Alexandre S. Leal[7], Paras N. Prasad[5], and Ronald L. Walsworth§[1,2,3,4]

[1]Quantum Technology Center, University of Maryland, College Park, MD 20742, USA

[2]Department of Electrical and Computer Engineering, University of Maryland, College Park, MD 20742, USA

[3]Department of Physics, University of Maryland, College Park, MD 20742, USA

[4]Joint Quantum Institute, University of Maryland, College Park, MD 20742, USA

[5]Institute for Lasers, Photonics and Biophotonics, and Department of Chemistry, University at Buffalo, State University of New York, Buffalo, NY 14260, USA

[6]Department of Physics, Federal University of Minas Gerais – UFMG, Belo Horizonte, MG, Brazil

[7]Nuclear Technology Development Center (CDTN), Belo Horizonte, MG, Brazil

*These authors contributed equally to this work.

†rescala1@umd.edu

‡abeling@umd.edu

§walsworth@umd.edu

A Systematic error investigations

A.1 Pulse spacing order

As our protocol relies on performing the same pulse sequence with many different spacings, we confirm that the order of these measurements does not impact the result by repeating the protocol 3 times using different measurement sequences on the same hBN flake.(Fig. S1). Measurement 1 was done by performing the measurements with separations from shortest to longest. Measurement 2 was done with separations going from longest to shortest, and measurement 3 was done with random pulse spacings. All three measurements are in agreement within the errors.

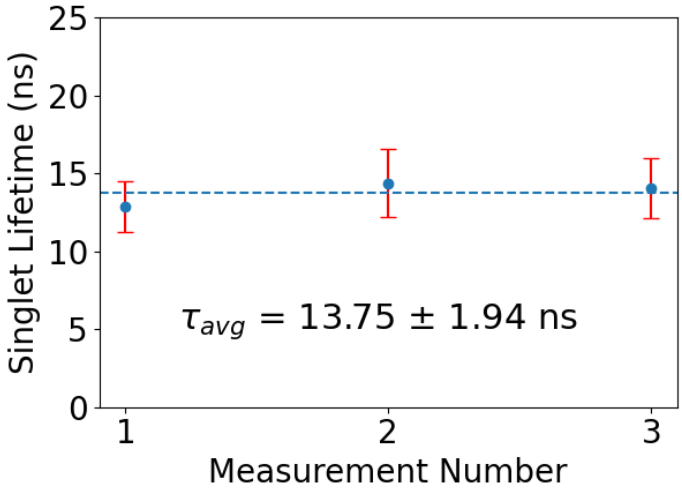


Figure S1: Singlet lifetime measurements on the same hBN flake while varying pulse spacing order.

A.2 Laser power

To investigate the laser excitation power dependence of the singlet lifetime measurement, we perform three measurements at different laser powers for both a large hBN flake ($>$ 1 μm) and a sub-micron flake. Figure S2a shows the data for the large flake, which exhibits a decrease in singlet lifetime with increasing power. For sub-micron flakes, the singlet lifetime shows no significant variation with laser power (Fig S2b).

Additionally, Figure S3 shows PL emission spectra for a sub-micron hBN flake at three laser excitation powers. We do not observe an increase in PL emission as a function of laser power in the range of ∼675-775 nm, as found for flakes $>1\mu$m (see Fig. 5 of the main text).

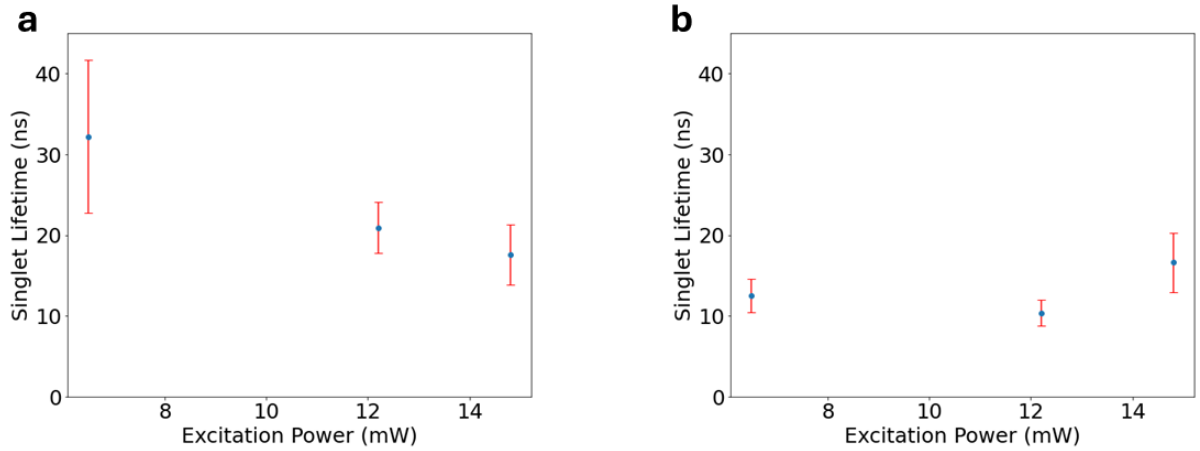


Figure S2: a) Singlet lifetime for a large hBN flake (> 1 μm) as a function of laser excitation power. b) Singlet lifetime for a sub-micron flake as a function of excitation power.

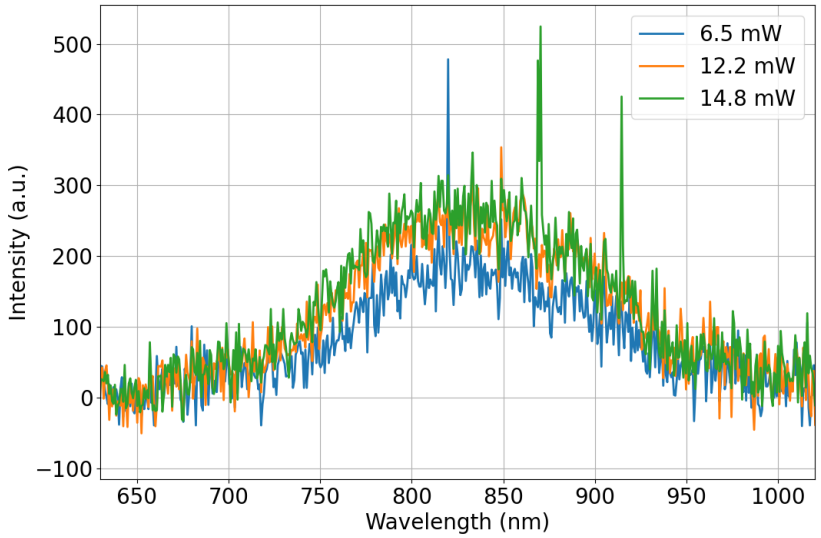


Figure S3: PL emission spectra for three laser excitation powers for a sub-micron hBN flake.

A.3 Laser Rise-Time

Figure S4 shows the rise-time of our laser as measured by a photodiode placed before the objective in the experimental setup and recorded on a fast oscilloscope (Rigol DHO4804). The measurements demonstrate that the laser rise-time is shorter than the bin width (5 ns) of the oscilloscope.

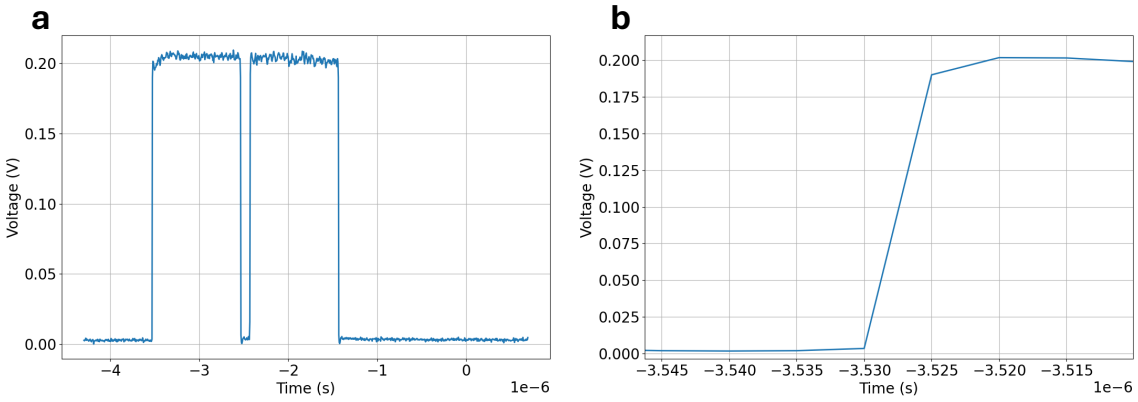


Figure S4: a) Laser pulse temporal profile measured using a fast oscilloscope and a photodiode placed before the objective. b) Zoomed-in of laser pulse rising edge showing the rise-time is shorter than the 5 ns bin width of the oscilloscope.

B Extraction of Electronic Transition Rates from Energy Level Model Fitting

B.1 7-level model

We fit time-resolved PL data from thermal and polarized V_B^- spin distributions. Transition rates for the 7-level model are shown in Fig. 1 of the main text and quantified in the linear, coupled set of ordinary differential equations (ODEs) below:

$$\begin{aligned}
\frac{dP_1}{dt} &= -(k_p + \frac{2k_{sd}}{3})P_1 + \frac{k_{sd}}{3}P_2 + \frac{k_{sd}}{3}P_3 + k_r P_4 + \kappa_0 P_7 \\
\frac{dP_2}{dt} &= \frac{k_{sd}}{3}P_1 - \left(k_p + \frac{k_{sd}}{3}\right)P_2 + k_r P_5 + \kappa_1 P_7 \\
\frac{dP_3}{dt} &= \frac{k_{sd}}{3}P_1 - \left(k_p + \frac{k_{sd}}{3}\right)P_3 + k_r P_6 + \kappa_1 P_7 \\
\frac{dP_4}{dt} &= k_p P_1 - (k_r + \gamma_0)P_4 \\
\frac{dP_5}{dt} &= k_p P_2 - (k_r + \gamma_1)\,P_5 \\
\frac{dP_6}{dt} &= k_p P_3 - (k_r + \gamma_1)\,P_6 \\
\frac{dP_7}{dt} &= \gamma_0 P_4 + \gamma_1 P_5 + \gamma_1 P_6 - (\kappa_0 + 2\kappa_1)P_7.
\end{aligned} \tag{S1}$$

Here, the rates γ_0 and γ_1 represent non-radiative population transfer to the shelving singlet state from the $m_s = 0$ and $m_s = \pm 1$ excited states, respectively. Likewise, κ_0 and κ_1 govern population transfer from the singlet state to the $m_s = 0$ and $m_s = \pm 1$ ground states, respectively. The optical pumping rate, k_p, is proportional to incident laser power, P, and quantifies spin conserving population transfer from the ground state triplet to the excited state triplet. In the 7-level model fit, we extract the scaling of this rate with power, k_{p_0}, such that $k_p = P \cdot k_{p_0}$. k_r quantifies the spin conserving radiative decay from the excited state triplet to the ground state triplet. We set k_r based on the *ab initio* DFT prediction of the radiative decay rate [1]. We incorporate single quantum longitudinal relaxation between spin sub-levels through the k_{sd} rate [2], which is proportional to the inverse of the T_1 time, and was previously measured to be approximately 13-19 μs [3, 4]. Fits are not sensitive to T_1 values within this range; therefore T_1 is fixed to 15 μs. We find that the time-resolved PL data do not uniquely constrain the absolute magnitudes of γ_0 and γ_1, whereas the ratio γ_0/γ_1 converges robustly across initializations; therefore, either γ_0 or γ_1 must be constrained by an independent measurement. We fix γ_0 using a literature average of directly measured $m_s = 0$ excited-state lifetimes, τ_0 [5, 6, 7], and treat the ratio γ_0/γ_1 as a fit parameter, from which γ_1 is inferred. Using $\tau_0 = 1/(k_r + \gamma_0)$, we compute $\gamma_0 = 1/\tau_0 - k_r$ (and note that $k_r \ll \gamma_0$ for the values used here).

With the above constraints, Eq. S1 is solved numerically, and the resultant normalized PL intensity over time at various powers is compared to time-resolved measurements for a global fit to extract the electronic transition rates of the intersystem crossing. The 7-level

model fit is in reasonable agreement with measurements on sub-micron hBN flakes for lower laser powers but fails at higher laser powers, as discussed in the main text. For example, as shown in Fig. 5 of the main text, the 7-level model fit fails to capture the dynamic and steady-state PL at the highest laser power (21.3 mW). The failure of the 7-level model with regard to steady state PL is particularly apparent in Fig. S5, where we show measured PL and fits to the 7-level model for the entire pulse sequence, rather than just for the first few hundred nanoseconds of each laser pulse.

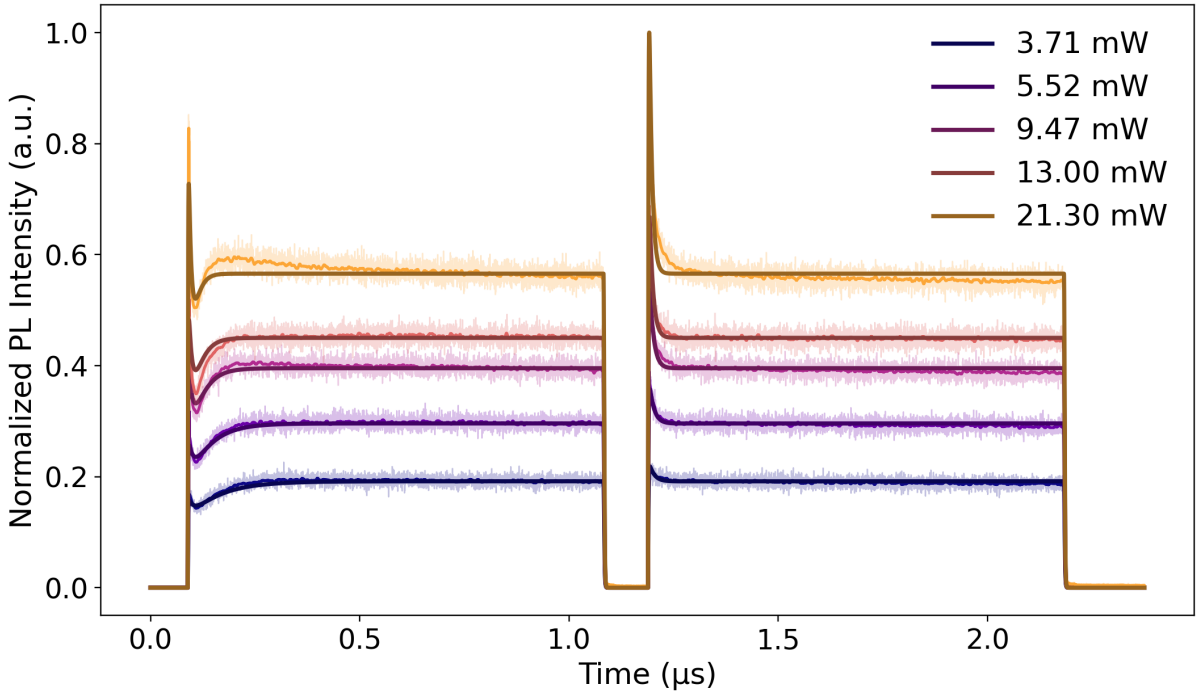


Figure S5: Measured PL time traces for a sub-micron hBN flake, following the measurement sequence described in Fig. 4a of the main text, showing thermal (left) and polarized (right) V_B^- spin distributions and fits to the 7-level model for five laser powers. Here, data and fits are shown from the full measurement sequence. The raw data is shown in a semi-opaque color scale compared to the smoothed data and fits (solid lines).

B.2 9-level model

Based on the poor fit at high laser power using the 7-level model, we introduce a 9-level model of V_B^- transition rates, which is shown diagrammatically in Fig. 4 of the main text. The dynamics of this expanded model are governed by the following set of 9 coupled ODEs describing population transfer between the boron vacancy's electronic energy levels:

$$
\begin{aligned}
\frac{dP_1}{dt} &= -(k_p + \frac{2k_{sd}}{3} + k_{di})P_1 + \frac{k_{sd}}{3}P_2 + \frac{k_{sd}}{3}P_3 + k_r P_4 + \kappa_0 P_7 + \frac{k_{dr}}{3}P_8 + k_{i2}P_9 \\
\frac{dP_2}{dt} &= \frac{k_{sd}}{3}P_1 - \left(k_p + \frac{k_{sd}}{3} + k_{di}\right)P_2 + k_r P_5 + \kappa_1 P_7 + \frac{k_{dr}}{3}P_8 + k_{i2}P_9 \\
\frac{dP_3}{dt} &= \frac{k_{sd}}{3}P_1 - \left(k_p + \frac{k_{sd}}{3} + k_{di}\right)P_3 + k_r P_6 + \kappa_1 P_7 + \frac{k_{dr}}{3}P_8 + k_{i2}P_9 \\
\frac{dP_4}{dt} &= k_p P_1 - (k_r + \gamma_0 + k_{i1})P_4 \\
\frac{dP_5}{dt} &= k_p P_2 - (k_r + \gamma_1 + k_{i1})\,P_5 \\
\frac{dP_6}{dt} &= k_p P_3 - (k_r + \gamma_1 + k_{i1})\,P_6 \\
\frac{dP_7}{dt} &= \gamma_0 P_4 + \gamma_1 P_5 + \gamma_1 P_6 - (\kappa_0 + 2\kappa_1)P_7 \\
\frac{dP_8}{dt} &= k_{i1}P_4 + k_{i1}P_5 + k_{i1}P_6 - (k_{dr} + k_{p2})P_8 + k_{di}P_1 + k_{di}P_2 + k_{di}P_3 + k_{nr}P_9 + k_{r2}P_9 \\
\frac{dP_9}{dt} &= k_{p2}P_8 - (3k_{i2} + k_{nr} + k_{r2})P_9
\end{aligned}
\tag{S2}
$$

Here, all transition rates from the 7-level model are retained and we add two additional levels, whose populations are denoted P_8 and P_9 in Eq. S2. We apply the same constraints on k_r, γ_0, and γ_1 as in the 7-level model: k_r is fixed to the *ab initio* DFT prediction, γ_0 is fixed using a literature average, and the ratio γ_0/γ_1 is treated as a fit parameter from which γ_1 is inferred. We insert several new transition rates between the two new levels. Firstly, we describe optical pumping between these two levels at a rate k_{p2}, which is linearly dependent on incident laser power, P, such that $k_{p2} = k_{p2_0} \cdot P$. In general, k_{p2} is not equal to k_p.

We model both radiative and non-radiative decay from level 9 (higher energy) to level 8 (lower energy), which are described by rates k_{r2} and k_{nr}, respectively. We also allow for photoconversion from the excited states of V_B^- to level 8, as well photorecombination from level 9 back to the V_B^- ground states. These two photo-driven processes are described by rates k_{i1} and k_{i2}, which both depend on incident laser power, P. We test multiple power dependency combinations for the photoconversion (k_{i1}) and photorecombination (k_{i2}) rates, and find best fits to the data for the combination where k_{i1} is quadratically dependent on power such that $k_{i1} = k_{i1_0} \cdot P^2$ and when k_{i2} is linearly dependent on power such that $k_{i2} = k_{i2_0} \cdot P$. Quadratic power-dependence of k_{i1} produces only modestly improved fits compared to linear dependence ($k_{i1} = k_{i1_0} \cdot P$), as quantified by the sum of square residuals or SSRs. To reflect this uncertainty, we run the full fitting procedure on both laser-power dependencies for k_{i1} (quadratic and linear) and incorporate the difference in fit parameters into the final reported uncertainties (see more details in section B.3).

We also incorporate dark conversion and recombination between the ground states of the 7 level system and the ground state of the additional 2 level system. These processes are quantified by rates k_{di} and k_{dr}, respectively. The transition rates k_{p2_0}, k_{r2}, k_{nr}, k_{i1_0}, and k_{i2_0} are initially kept as free parameters in the model. In all test fits to PL data, the dark transition rate k_{dr} is found to be very small, has negligible contribution to fit quality, and

is therefore fixed to 0 for simplicity. We note that a non-zero recombination pathway (k_{dr} and k_{i2_0}) from the 2 level system to the 7 level system is required to sustain a finite V_B^- population in the steady-state; however, the sensitivity of our model and data is insufficient to place meaningful bounds on these recombination rates.

We additionally test photo-assisted ground state and singlet state transition pathways to the 2 level system, as previously observed for the NV center in diamond with regard to photoionization from NV^- to NV^0[8, 9, 10]. In all test fits to PL data, the rates of these additional pathways converge to 0 and do not contribute to the overall fit quality compared to k_{i1}, and so the associated rate constants are fixed to 0 for the final fit. k_{i2_0} is found to be many orders of magnitude smaller than the other photo-assisted rates for all laser powers, does not robustly converge under the LHS scheme, and is therefore fixed to 0 in the final fitting procedure. The best fit values of all parameters are extracted from a global fit to our laser-power dependent datasets. PL data from the full measurement sequence (rather than just from the first few hundred nanoseconds of each laser pulse shown in the main text), along with 9-level model fits, are shown in Fig. S6.

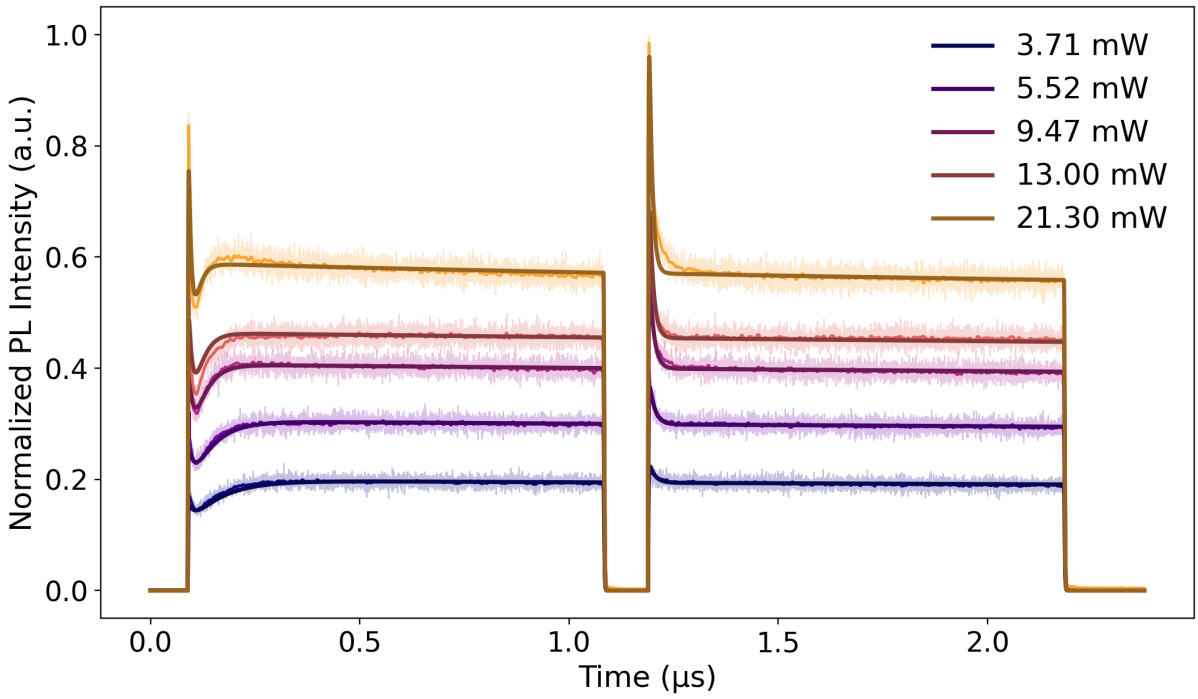


Figure S6: Measured PL time traces for a sub-micron hBN flake, following the measurement sequence described in Fig. 4a of the main text, showing thermal (left) and polarized (right) V_B^- spin distributions and fits to the 9-level model for five laser powers. Here, data and fits are shown from the full measurement sequence. The raw data is shown in a semi-opaque color scale compared to the smoothed data and fits (solid lines).

B.3 Details on fitting procedure and uncertainty estimation

We obtain rate estimates by minimizing the sum of squared residuals (SSR) between simulated and measured time-resolved PL traces across all time bins and all laser powers in a single global fit. Prior to fitting, the PL traces are globally normalized, as the absolute PL scale cannot be predicted without independent calibration of PL optical collection efficiency, laser illumination spot size, and emitter number. This global normalization enforces consistency of the relative PL scaling across laser powers. However, to account for observed PL drift in sub-diffraction-limited spots, including effects from laser power fluctuations, axial defocusing, and other collection efficiency variations, we include a per-power multiplicative factor e_{p_i} constrained to 0.9–1.1 (based on the typical amplitude of PL-scale fluctuations observed over the duration of our measurements). In the SSR-selected fits used in the procedure described below, e_{p_i} converged within the interval and did not reach the bounds. No additional weighting is applied across laser powers or time bins.

To reduce sensitivity to local minima, we perform a multi-start fit in which 250 initial parameter vectors are generated via Latin hypercube sampling (LHS) [11]. Transition rates and SSR are convergent within 250 initial parameter vectors; there is negligible improvement to SSR when the LHS procedure is extended to 1000 initial guesses. For rates with established bounds, the LHS ranges encompass literature values; for weakly constrained rates in this model, the ranges are widened to ensure broad coverage of plausible values. Certain rates that are found to be very small and do not meaningfully affect the fit (as described in section B.2) are fixed to zero. The measured PL traces are smoothed with a mean-shift filter for the final SSR comparison between the 9-level and 7-level model to remove shot noise; and for data visualization purposes. However, all fitting and uncertainty analysis are conducted on the raw PL data traces after global normalization.

Statistical uncertainties are estimated by bootstrap resampling. In this procedure, resampling and refitting are performed on the PL traces. In each resample, we select each of three LHS solutions with the lowest SSRs. For each timebin t_i with corresponding PL value y_i, synthetic data are drawn from a Poisson distribution with a mean $\lambda = y_i$, and the model is then refitted to this resampled dataset. Repeating this procedure 250 times yields parameter distributions from which 95% confidence intervals are extracted as measures of statistical uncertainty from photon shot-noise. The resulting uncertainties are negligibly small (typically $<1\%$), suggesting that photon shot-noise is not a limiting factor. Using alternative bootstrap schemes such as the wild bootstrap method [12] leads to the same result. The median parameter values obtained from the bootstrap procedure are consistent with the top LHS fits to the original data and are reported as the nominal rates in Tables 2 and 3 of the main text.

In order to capture systematic uncertainties beyond statistical noise, we perform jackknife resampling to calculate how much our fitted parameters change when data taken at any single laser power is excluded. This accounts for how much our results depend on specific choices of laser powers. This procedure results in parameter distributions across the jackknifed datasets, from which we extract the median absolute deviation (MAD) as a robust measure of spread. For the 7-level model, we convert this spread to a standard deviation (multiplying MAD by 1.4826) and add it in quadrature with the statistical uncertainty from the Poisson bootstrap procedure (assuming that statistical counting noise and finite laser power selection

are approximately independent contributions).

For the 9-level model, we estimate a third source of uncertainty from the a priori unknown dependence on laser power, P, of photo-assisted conversion pathways between the 7 level and 2 level systems, as discussed in B.2 above. Using the LHS procedure, linear dependence on laser power (i.e., $k_{i1} = k_{i1_0} \cdot P$) is found to produce slightly poorer SSRs than quadratic dependence on laser power (i.e., $k_{i1} = k_{i1_0} \cdot P^2$), although variation in fitted rates is within the uncertainties described above. A possible physical picture for the improved fits to PL data provided by the 9 level model at high laser power is photoionization from V_B^- (described by the 7 level system) to V_B^0 (approximately described by the 2 level system). In the literature to date, however, there is no ionization threshold energy measurement; and charge-transition level calculations can plausibly support both two-photon and one-photon photoionization from the V_B^- excited state [13, 14]. Lacking a definitive answer to this open question, we elect to report the nominal rates for fits using quadratic laser-power dependence, but include variations in the fitted rates between the two forms (quadratic and linear power dependence) as part of our uncertainty budget. The resulting uncertainty is added in quadrature to the statistical and systematic uncertainties described in previous paragraphs to result in the final uncertainty displayed in Table 3 of the main text.

C 5-Level vs. 7-Level Model

We note that the 5-level model (used in [6] and [15]) is functionally equivalent to the 7-level model (used in this work, in [16], and in [7]), since the V_B^- $m_s = +1$ and $m_s = -1$ are assumed to be indistinguishable. This equivalence is evident in Eq. S1 and Eq. S2, where the population transfer rates for the $m_s = +1$ and $m_s = -1$ are identical. We note, however, that the transfer rate, κ_1 from the singlet state to the $m_s = \pm 1$ ground state energy levels must be multiplied by two to convert from the 7-level rate to the 5-level rate. This factor is needed because the $m_s = \pm 1$ populations are combined into a single level for the 5-level model, and so experience twice as much population transfer from the singlet to the combined energy level as compared to the 7-level model, where the $m_s = +1$ and $m_s = -1$ populations are not combined. In other words, the singlet state transfers to two distinct energy levels in the 5-level model and three distinct energy levels in the seven level model. Mathematically, $\kappa_{1_{fivelevel}} = 2\kappa_{1_{sevenlevel}}$ and $\tau_s = \frac{1}{\kappa_0 + 2\kappa_{1_{sevenlevel}}} = \frac{1}{\kappa_0 + \kappa_{1_{fivelevel}}}$.

We express all rates in Table 2 of the main text in terms of the 7-level model, meaning κ_1 as reported in [6] and [15] is divided by two.

D Impact of Laser Rise-Time on Normalized PL Predictions

We simulate the variation in PL dynamics as a function of laser rise-time using the 7-level rate equation model. We use an optical pumping rate of 20 MHz and electronic transition rates reported in [5] . Then, we allow k_p to rise or fall to its maximum or minimum value over the course of a specified rise/fall time corresponding to incident laser pulses. The calculated

PL response from a polarized V_B^- spin distribution to pulses with 0, 2, 30, and 50 ns rise-times is shown in Fig. S7. For a 2 ns rise-time, the calculated PL nearly matches the PL for an instantaneous (i.e. 0 ns) rise-time. By contrast, the calculated PL for 30 and 50 ns rise-times drastically underestimates the transient PL peak compared to the instantaneous and 2 ns rise-times. Rise-times on the order of 30-50 ns are typical of AOM-based laser pulses, while the modulated laser diode technology used in the present work allows for a laser rise-time of $<$2.5 ns. The fast rise-times of our laser therefore allow us to probe the early photophysics dynamics of V_B^- ensembles in hBN more accurately than previous studies relying on an AOM.

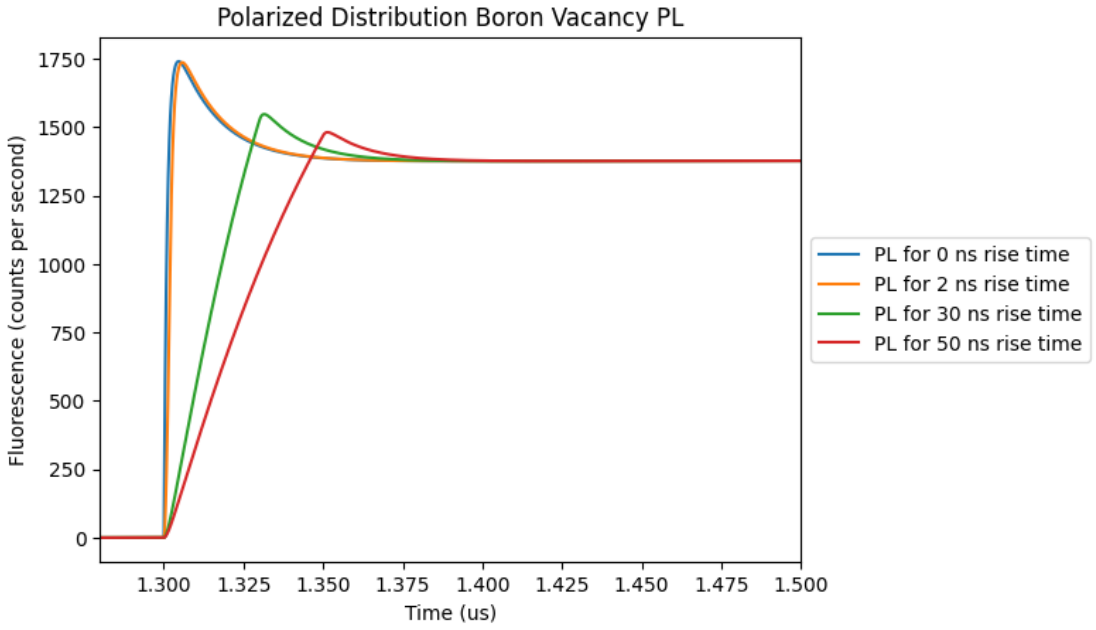


Figure S7: PL calculated with the 7-level model for an $m_s = 0$ polarized V_B^- spin distribution for various optical pumping rate rise-times.

E Polarization to the Singlet State

We characterize the variation between sub-micron hBN flakes of V_B^- polarization to the singlet state for ≈13.8 mW of 515 nm laser excitation power (measured at the sample). Measurements are performed for a 2 μs laser pulse, with lower bound on singlet state polarization the contrast of observed dynamic PL peak height to the steady state PL value (Fig S8a). The mean PL peak contrast for the 16 measured flakes ≈42% with a standard deviation of 1% (Fig S8b). This contrast can only be accurately measured using laser excitation with fast rise times (∼2.5 ns), since using an AOM to modulate laser excitation would result in an underestimation of V_B^- polarization (see Fig. S7). It should be noted that singlet state polarization is laser-power dependent. Additionally, the 9-level model suggests that the singlet state may not be the only dark state accessible to boron vacancy defects under laser illumination.

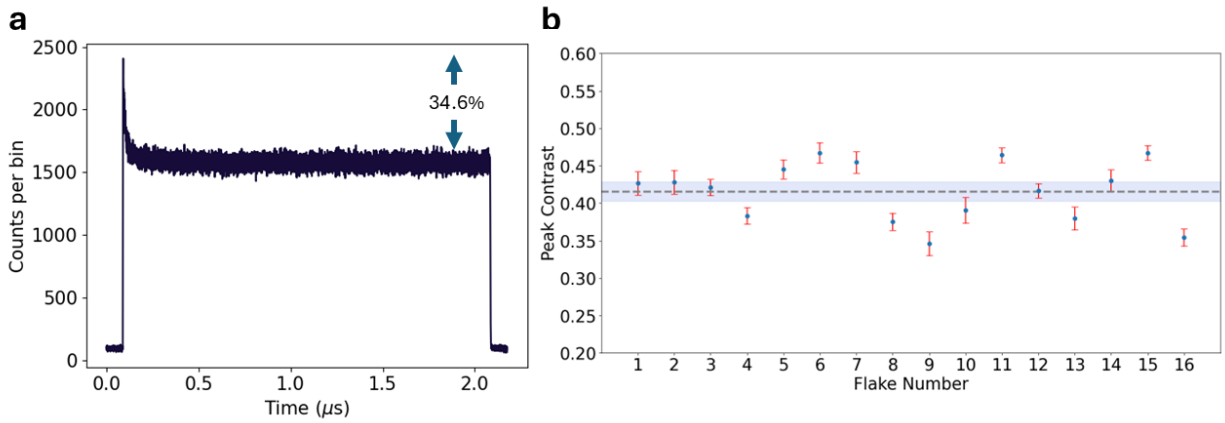


Figure S8: a) Example measured contrast of dynamic PL peak height to the steady state PL value, during a 2 μs laser pulse, gives a lower bound of V_B^- polarization to the singlet state in a single sub-micron hBN flake. b) Experimentally-determined peak contrast values for each of 16 sub-micron flakes. The dashed line designates the mean peak contrast ≈42% and the shaded region is 1 standard deviation of the mean.

F Optical Images of hBN Flakes

Optical images (Fig. S9) indicate that larger hBN flakes could be aggregates of smaller flakes. Further investigation is warranted of the effects of hBN flake size and potential flake aggregation and other properties (e.g., strain, edge effects) on observed V_B^- and other emitter properties.

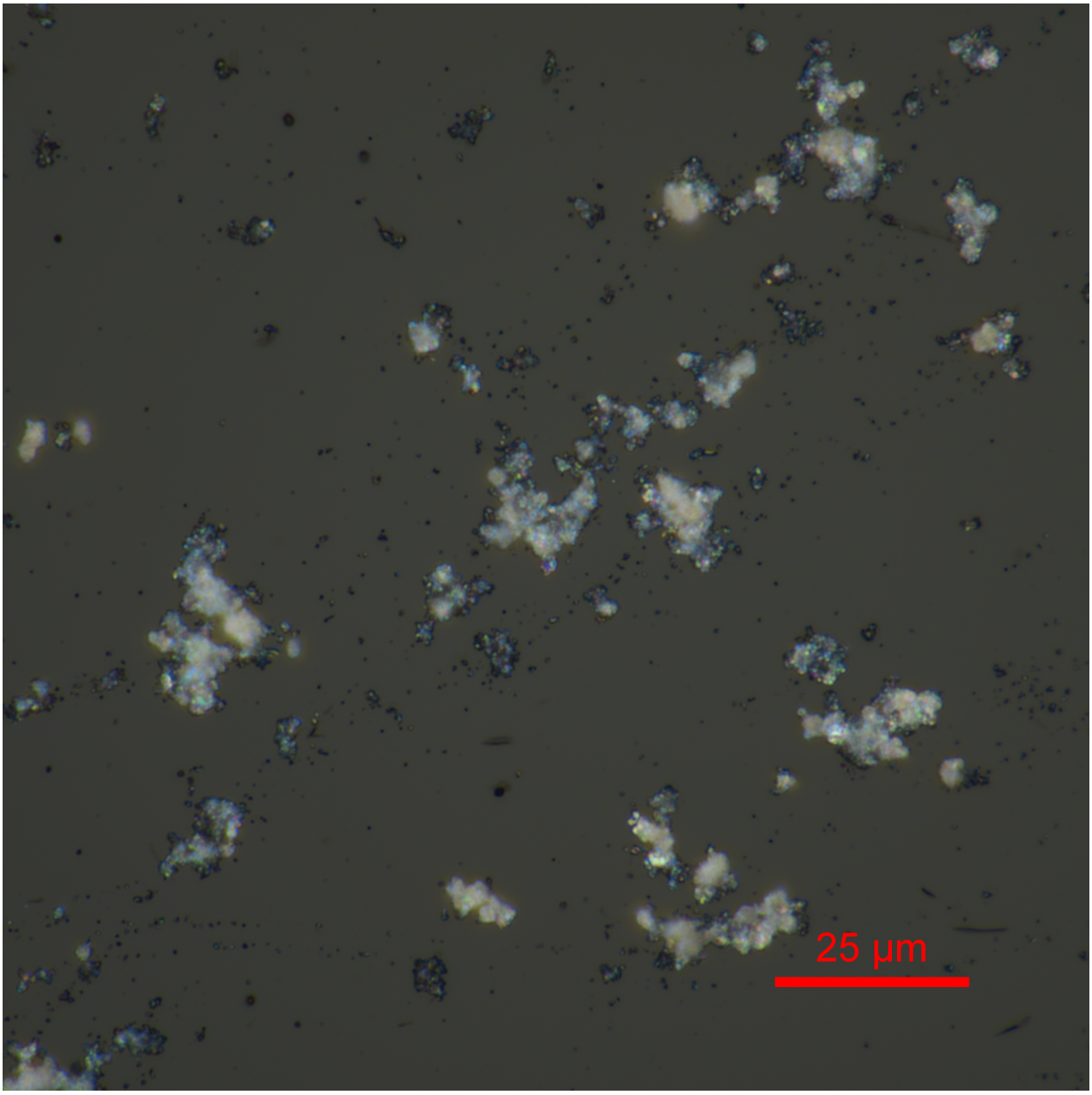


Figure S9: Optical images of dropcast hBN flakes used in this study.

References

[1] Jeffrey R. Reimers, Jun Shen, Mehran Kianinia, Carlo Bradac, Igor Aharonovich, Michael J. Ford, and Piotr Piecuch. Photoluminescence, photophysics, and photochemistry of the $V_B{}^-$ defect in hexagonal boron nitride. *Phys. Rev. B*, 102:144105, Oct 2020.

[2] B. A. Myers, A. Ariyaratne, and A. C. Bleszynski Jayich. Double-quantum spin-relaxation limits to coherence of near-surface nitrogen-vacancy centers. *Phys. Rev. Lett.*, 118:197201, May 2017.

[3] A. Durand, T. Clua-Provost, F. Fabre, P. Kumar, J. Li, J. H. Edgar, P. Udvarhelyi, A. Gali, X. Marie, C. Robert, J. M. Gérard, B. Gil, G. Cassabois, and V. Jacques. Optically active spin defects in few-layer thick hexagonal boron nitride. *Phys. Rev. Lett.*, 131:116902, Sep 2023.

[4] Andreas Gottscholl, Matthias Diez, Victor Soltamov, Christian Kasper, Andreas Sperlich, Mehran Kianinia, Carlo Bradac, Igor Aharonovich, and Vladimir Dyakonov. Room temperature coherent control of spin defects in hexagonal boron nitride. *Science Advances*, 7(14):eabf3630, 2021.

[5] T. Clua-Provost, Z. Mu, A. Durand, C. Schrader, J. Happacher, J. Bocquel, P. Maletinsky, J. Fraunié, X. Marie, C. Robert, G. Seine, E. Janzen, J. H. Edgar, B. Gil, G. Cassabois, and V. Jacques. Spin-dependent photodynamics of boron-vacancy centers in hexagonal boron nitride. *Phys. Rev. B*, 110:014104, Jul 2024.

[6] Simon Baber, Ralph Nicholas Edward Malein, Prince Khatri, Paul Steven Keatley, Shi Guo, Freddie Withers, Andrew J. Ramsay, and Isaac J. Luxmoore. Excited state spectroscopy of boron vacancy defects in hexagonal boron nitride using time-resolved optically detected magnetic resonance. *Nano Letters*, 22(1):461–467, December 2021.

[7] W. Lee, V. S. Liu, Z. Zhang, S. Kim, R. Gong, X. Du, K. Pham, T. Poirier, Z. Hao, J. H. Edgar, P. Kim, C. Zu, E. J. Davis, and N. Y. Yao. Intrinsic high-fidelity spin polarization of charged vacancies in hexagonal boron nitride. *Phys. Rev. Lett.*, 134:096202, Mar 2025.

[8] N Aslam, G Waldherr, P Neumann, F Jelezko, and J Wrachtrup. Photo-induced ionization dynamics of the nitrogen vacancy defect in diamond investigated by single-shot charge state detection. *New Journal of Physics*, 15(1):013064, jan 2013.

[9] Sean M. Blakley, Thuc T. Mai, Stephen J. Moxim, Jason T. Ryan, Adam J. Biacchi, Angela R. Hight Walker, and Robert D. McMichael. Spectroscopy of photoionization from the ^1e singlet state in nitrogen-vacancy centers in diamond. *Phys. Rev. B*, 110:134109, Oct 2024.

[10] Kristine V. Ung, Connor A. Roncaioli, Ronald L. Walsworth, and Sean M. Blakley. High resolution temperature-resolved spectroscopy of the nitrogen vacancy ^1e singlet state ionization energy, 2025.

[11] M. D. Mckay, R. J. Beckman, and W. J. Conover. A Comparison of Three Methods for Selecting Values of Input Variables in the Analysis of Output From a Computer Code. *Technometrics*, 42(1):55–61, February 2000. Publisher: ASA Website _eprint: https://www.tandfonline.com/doi/pdf/10.1080/00401706.2000.10485979.

[12] C. F. J. Wu. Jackknife, Bootstrap and Other Resampling Methods in Regression Analysis. *The Annals of Statistics*, 14(4):1261–1295, December 1986.

[13] L. Weston, D. Wickramaratne, M. Mackoit, A. Alkauskas, and C. G. Van de Walle. Native point defects and impurities in hexagonal boron nitride. *Phys. Rev. B*, 97:214104, Jun 2018.

[14] Jack Strand, Luca Larcher, and Alexander L Shluger. Properties of intrinsic point defects and dimers in hexagonal boron nitride. *Journal of Physics: Condensed Matter*, 32(5):055706, nov 2019.

[15] Benjamin Whitefield, Milos Toth, Igor Aharonovich, Jean-Philippe Tetienne, and Mehran Kianinia. Magnetic field sensitivity optimization of negatively charged boron vacancy defects in hbn. *Advanced Quantum Technologies*, July 2023.

[16] Tristan Clua-Provost, Alrik Durand, Jules Fraunié, Cédric Robert, Xavier Marie, Jiahan Li, James H. Edgar, Bernard Gil, Jean-Michel Gérard, Guillaume Cassabois, and Vincent Jacques. Impact of thickness-dependent nanophotonic effects on the optical response of color centers in hexagonal boron nitride. *Nano Letters*, October 2024.